Contributions of the Protein Environment to the Midpoint Potentials of the A_1 Phylloquinones and the F_X Iron−Sulfur Cluster in Photosystem I†

Irina Karyagina,[‡] Yulia Pushkar,[‡,§] Dietmar Stehlik,[‡] Art van der Est,[∥] Hiroshi Ishikita,[⊥,#] Ernst-Walter Knapp,[⊥] Bharat Jagannathan,[▽] Rufat Agalarov,[▽] and John H. Golbeck*[,▽,○]

Institut für Experimentalphysik, Freie Universität Berlin, Arnimallee 14, D-14195, Berlin, Germany, Department of Chemistry, Brock University, 500 Glenridge Avenue, St. Catharines, Ontario, L2S 3A1, Canada, Department of Biology, Chemistry and Pharmacy, Institute of Chemistry and Biochemistry, Freie Universität Berlin, Takustrasse 6, Berlin D-14195, Germany, Department of Biochemistry and Molecular Biology, Pennsylvania State University, University Park, Pennsylvania 16802, and Department of Chemistry, Pennsylvania State University, University Park, Pennsylvania 16802

Received May 4, 2007; Revised Manuscript Received June 28, 2007

ABSTRACT: Electrostatic calculations have predicted that the partial negative charge associated with $D575_{PsaB}$ plays a significant role in modulating the midpoint potentials of the A_{1A} and A_{1B} phylloquinones in photosystem I. To test this prediction, the side chain of residue 575_{PsaB} was changed from negatively charged (D) to neutral (A) and to positively charged (K). $D566_{PsaB}$, which is located at a considerable distance from either A_{1A} or A_{1B}, and should affect primarily the midpoint potential of F_X, was similarly changed. In the 575_{PsaB} variants, the rate of electron transfer from A_{1A} to F_X is observed to decrease slightly according to the sequence D/A/K. In the 566_{PsaB} variants, the opposite effect of a slight increase in the rate is observed according to the same sequence D/A/K. These results are consistent with the expectation that changing these residues will shift the midpoint potentials of nearby cofactors to more positive values and that the magnitude of this shift will depend on the distance between the cofactors and the residues being changed. Thus, the midpoint potentials of A_{1A} and A_{1B} should experience a larger shift than will F_X in the 575_{PsaB} variants, while F_X should experience a larger shift than will either A_{1A} or A_{1B} in the 566_{PsaB} variants. As a result, the driving energy for electron transfer from A_{1A} and A_{1B} to F_X will be decreased in the former and increased in the latter. This rationalization of the changes in kinetics is compared with the results of electrostatic calculations. While the altered amino acids shift the midpoint potentials of A_{1A}, A_{1B}, and F_X by different amounts, the difference in the shifts between A_{1A} and F_X or between A_{1B} and F_X is small so that the overall effect on the electron transfer rate between A_{1A} and F_X or between A_{1B} and F_X is predicted to be small. These conclusions are borne out by experiment.

In oxygenic photosynthesis, photosystem I (PS I[1]) participates in the conversion of light into chemical energy by generating a strong reductant, NADPH. The reducing potential required for this process is generated by light-induced electron transfer along a series of cofactors bound to the PsaA and PsaB subunits of PS I (see ref (*1*) for recent reviews). The primary process of charge separation culminates with a hole at the primary donor P_{700} (a Chl *a*/Chl *a*′ heterodimer) and an electron at the primary acceptors A_{0A}/A_{0B} (each a Chl *a* monomer). This initial charge separated state is stabilized by electron transfer to the secondary acceptors A_{1A}/A_{1B} (phylloquinone) and to F_X (a $[4Fe\text{-}4S]^{1+,2+}$ cluster ligated between the PsaA/PsaB heterodimer). Two additional $[4Fe\text{-}4S]^{1+,2+}$ clusters, F_A and F_B, which are bound to the PsaC subunit, act as terminal acceptors.

Spectroscopic and structural studies have revealed two prominent features of the electron transfer cofactors. First, they are arranged in two nearly C_2-symmetric branches extending from the common donor P_{700} and converging at the iron−sulfur (Fe/S) cluster F_X. Thus, there appears to be redundancy in the electron transfer pathway. Following a line of reasoning first proposed by Joliot and Joliot (*2*) and later supported by optical studies of site-directed mutants in eukaryotes (*3*) and prokaryotes (*4*), two discrete kinetic events are attributed to the oxidation of the two phylloquinones in PS I. The fast (τ = 7 to 20 ns) and slow (τ =150 to

† Supported by DFG, Sfb 498, A3 and A5, the US National Science Foundation (MCB-0519743), the Natural Sciences and Engineering Research Council of Canada, and the Japan Society for the Promotion of Science (JSPS) fellowship for research abroad.

* Corresponding author: Department of Biochemistry and Molecular Biology, Pennsylvania State University, University Park, PA 16802. Tel: 1 814 865 1163. Fax: 1 814 865 1163. E-mail: jhg5@psu.edu.

‡ Institut für Experimentalphysik, Freie Universität Berlin.

§ Present address: Melvin Calvin Laboratory, Physical Biosciences Division, Lawrence Berkeley National Laboratory, Berkeley, CA 94720-5230.

∥ Brock University.

⊥ Institute of Chemistry and Biochemistry, Freie Universität Berlin.

Present address: 417 SGM Building, Department of Chemistry, University of Southern California, Los Angeles, CA 90089.

▽ Department of Biochemistry and Molecular Biology, Pennsylvania State University.

○ Department of Chemistry, Pennsylvania State University.

[1] Abbreviations: A_{1A}, PsaA-branch phylloquinone; A_{1B}, PsaB-branch phylloquinone; Chl, chlorophyll; Chl *a*′, 13^2 epimer of Chl *a*; ENDOR, electron nuclear double resonance; EPR, electron paramagnetic resonance; ESEEM, electron spin echo envelope modulation; Fe/S, iron−sulfur; F_X, interpolypeptide Fe/S cluster shared by PsaA and PsaB; NaAsc, sodium ascorbate; PS I, photosystem I; TR EPR, transient EPR.

10.1021/bi700846z CCC: $37.00
Published on Web 08/29/2007

300 ns) kinetic phases are assigned to electron transfer through the PsaB-branch and PsaA-branch of electron transfer cofactors, respectively. We follow this convention here and assign the fast kinetic phase to the oxidation of A_{1B}^- and the slow kinetic phase to the oxidation of A_{1A}^-. Note, however, that unlike PS I in *Chlorella* or *Chlamydomonas reinhardtii*, electron transfer is highly asymmetrical in *Synechocystis* sp. PCC 6803, with the majority of the electron flux passing through the PsaA-branch of cofactors (*5*−*9*). Second, the reduction potentials of the acceptors, in particular those of the two quinones, A_{1A} and A_{1B}, are highly negative. However, the precise midpoint potentials of the quinone/semiquinone anion radical pair in the A_{1A} and A_{1B} sites have not been measured directly. In years past when no distinction was made between the two branches, the midpoint potential of "A_1" was estimated to range from −760 mV (*10*) to −820 mV (*11*), making this site one of the most reducing environments for a quinone in all of biology. To the extent that Marcus theory describes the relationship between the rate of electron transfer and the change in Gibbs free energy between an electron donor and acceptor pair (*12*), a shift in the midpoint potential of a given cofactor can be monitored indirectly by a change in the rate of reduction and/or oxidation of either the donor or acceptor (*13*, *14*). Therefore, measuring the kinetics of A_{1A}^- and A_{1B}^- oxidation provides a means to monitor changes in the midpoint potential difference between the quinones and the F_X cluster, with the caveat that factors such as changes in distance, orientation, and reorganization energy remain unaltered.

Several spectroscopic techniques, including transient EPR (TR EPR) and time-resolved optical spectroscopy, have been used to study the influence of amino acids involved in cofactor−protein interactions along the putative electron transfer pathway from P_{700} to F_X (*3*, *7*, *8*, *15*−*17*). The initial goal of these studies was to identify which of the two quinones were associated with the optical and EPR spectroscopic signatures of "A_1". In the course of these studies, important questions have been raised regarding the influence of the protein on the midpoint potentials of both A_{1A} and A_{1B}. Two of the amino acids targeted earlier for mutagenesis were $W697_{PsaA}$ and $W677_{PsaB}$, which are π-stacked with the respective quinones, and $S692_{PsaA}$ and $S672_{PsaB}$, which are H-bonded to the respective Trp residues as well as the backbone of the $M688_{PsaA}$ and $M668_{PsaB}$ ligands to A_{0A} and A_{0B}. The striking result was that alteration of these otherwise critical amino acids had only a modest effect on the rate of electron transfer from A_{1A}^- (the slow kinetic phase) and A_{1B}^- (the fast kinetic phase) to F_X (*3*, *7*, *8*) despite the fact that their side groups are either in direct or indirect van der Waals contact with the quinone.

With the availability of the X-ray crystal structure of cyanobacterial PS I at 2.5 Å resolution (*18*), it has become possible to use computational techniques to study the electrostatic environment of the electron transfer cofactors (*19*, *20*). An important aspect of these theoretical studies is that they make predictions about the role of specific features of the structure in modulating the midpoint potentials of the cofactors. Hence, they provide a guide for designing experimental strategies intended to probe the electrostatic environment. The electrostatic calculations for the quinone sites in PS I (*19*) indicate that the modest effect on electron transfer in the variants described above may be because the side groups of these residues cause only minor shifts of the quinone midpoint potential. For example, setting of the local charges on $W697_{PsaA}$ and $W677_{PsaB}$ to zero produced an identical shift of only −27 mV in the midpoint potentials of A_{1A} and A_{1B}. These computational studies have addressed additional questions: (i) What is the origin of the highly negative midpoint potential of the A_{1A} and A_{1B} quinones? (ii) What is the explanation for the putative difference in the midpoint potentials of A_{1A} and A_{1B} in the two branches? (iii) How are the various calculated contributions to the electrostatic environment reflected in the electron transfer kinetics from A_{1A} and A_{1B} to F_X? Although there may be significant spread (uncertainty) in the calculated quinone midpoint potentials because they depend critically on specific structural and electrostatic properties, the calculations pointed clearly to the influence of the charge (formally −2) on the F_X cluster as a major contributor (i.e., a 240 mV to 260 mV downward shift) to the highly negative potential of A_{1A} and A_{1B} (*19*)). (Note that removal of the charge associated with the F_X cluster in the *rubA* variant did not result in a sufficient reduction of the driving force to slow down the forward ET rates *to* the A_1 acceptor such that the change in rate would be detectable by TR EPR (*21*, *22*). However, it should be kept in mind that the net positive charges from amino acids in the F_X environment might be partially compensated by subsequent deprotonation of those residues due to solvent exposure after removal of F_X.) Another strong contributor was predicted to be the PsaB specific residue $D575_{PsaB}$, but the magnitude of the effect depends on its protonation state. The midpoint potential of A_{1B} was predicted to be ∼150 mV more negative than that of A_{1A}, primarily because $D575_{PsaB}$ couples more strongly to A_{1A} and because the different backbone conformations of PsaA and PsaB, namely, from $S692_{PsaA}$ and $S672_{PsaB}$, stabilize the two quinones by different amounts (*19*). Indeed, the more positive potential of A_{1A} is in agreement with the slower kinetics of electron transfer to F_X.

The precise relationship between various contributions to the midpoint potentials and the electron transfer kinetics are understandably difficult to evaluate (*23*). However, the usefulness of the electrostatic calculations can be evaluated by using the detailed predictions of the individual influences (direct and indirect) of specific charges (amino acid side chains, degree of protonation of charged side chains, amino acid backbone dipoles, cofactors, ions, etc.) on the midpoint potential of a specific cofactor to design and interpret point mutation experiments. In particular, the role of the side chain of the Asp residues in positions 575_{PsaB} and 566_{PsaB} was targeted in this study. Because $D575_{PsaB}$ has been proposed to play such a crucial role in lowering the midpoint potential (which is expected to modulate the electron transfer rate), we focus first on this residue. The position of $D575_{PsaB}$ and the symmetry related residue $Q588_{PsaA}$ in the immediate environment of the $A_{1A/B}$ and F_X cofactors is shown in Figure 1 as provided by the structural model of the PS I complex at 2.5 Å resolution (PDB entry 1JB0). Viewed both along the membrane normal and in the plane of the membrane, it is apparent that $D575_{PsaB}$ is located considerably closer to A_{1A} than to A_{1B}. This suggests that any electrostatic influences due to this residue will be more prominent for A_{1A} than for A_{1B}. Indeed, the reduction of A_{1A} is predicted

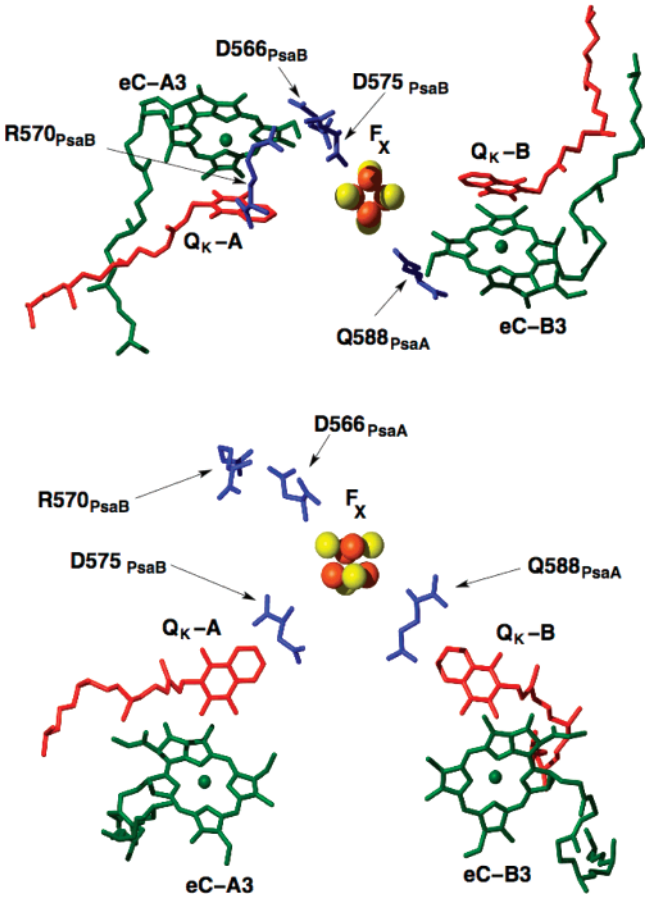

FIGURE 1: The arrangement of the cofactors in PS I in the region of the stromal acceptors A_{1A}, A_{1B}, and F_X shown from two perspectives. The locations of the residues $D575_{PsaB}$, $D566_{PsaB}$, $R570_{PsaB}$, and $Q588_{PsaA}$ are also indicated. The first three of these residues were targeted for mutation while $Q588_{PsaA}$ is the residue in PsaA that is analogous to $D575_{PsaB}$ in PsaB. The top panel is a view from the stromal side of the complex along the membrane normal. The bottom panel is a view along a direction approximately perpendicular to the membrane normal. In both cases the PsaA-branch of cofactors is on the left and the PsaB-branch is on the right.

to cause a larger protonation of $D575_{PsaB}$ than does the reduction of A_{1B} (*19*). The difference in Gibbs free energy determines the net driving energy for the forward electron transfer kinetics from A_{1A} and A_{1B} to F_X. Therefore, it is equally important to determine the relative midpoint potential shifts for F_X as well as A_{1A}/A_{1B}. The midpoint potential shift in F_X was not specified in ref *19*, but it is considered explicitly here, in particular in relation to the midpoint potential shifts in A_{1A}/A_{1B}.

In this paper, we test the hypothesis that the PsaB specific D575 residue has a significant effect on the midpoint potentials of A_{1A} and A_{1B} by studying the influence of changes in the identity of the side chain on the rate of electron transfer from A_{1A}/A_{1B} to F_X. To generate the largest possible range of differences, the Asp has been changed to Ala with a neutral side chain and to Lys with a side chain that is positively charged in solvent at an appropriate pH. In addition, $R570_{PsaB}$ and $D566_{PsaB}$ were also targeted for mutagenesis. Together with the symmetry related PsaA analogue $D579_{PsaA}$, the two targeted residues play a key role in the network of ionic interactions that constitute the interface between the PsaB/PsaA heterodimer and the stromal protein subunit PsaC. (See ref *24* for a detailed analysis.) $D566_{PsaB}$ is involved in salt-bridges to $R65_{PsaC}$ and $K51_{PsaC}$; its negative charge is compensated in the wild-type, but its replacement with Ala and Lys may leave an uncompensated positive charge on both $R65_{PsaC}$ and $K51_{PsaC}$. Because $D566_{PsaB}$ is located at the stromal surface and at a considerable distance from either A_{1A} or A_{1B}, the uncovering of these positive charges should affect primarily the midpoint potential of F_X. A variant of $R570_{PsaB}$ is employed as a control. Along with $R65_{PsaC}$, $R570_{PsaB}$ is salt-bridged to OD2 of $D566_{PsaB}$ (OD1 is salt-bridged to $K51_{PsaC}$) and is H-bonded to the backbone oxygen of $L552_{PsaB}$. It stabilizes the network of ionic interactions at the above-mentioned stromal interface. When this Arg is changed to Glu ($R570E_{PsaB}$), it does not uncover an uncompensated charge. Because it is sufficiently distant from F_X and A_{1A}/A_{1B}, the replacement of a basic group with an acidic side group is not expected to have a significant effect on the midpoint potentials of either the A_{1A}/A_{1B} quinones or the F_X Fe/S cluster. The experimental kinetics results are compared with additional electrostatic calculations that take into account the influence of $D575_{PsaB}$ and $D566_{PsaB}$ on the midpoint potentials of the F_X cluster as well as the quinones in the A_{1A} and A_{1B} sites.

MATERIALS AND METHODS

Preparation and Characterization of the $D575_{PsaB}$ and $D566_{PsaB}$ Variants. The $D566K_{PsaB}$, $D566A_{PsaB}$, $D557K_{PsaB}$, $D557A_{PsaB}$, and $R561E_{PsaB}$ variants of *Synechocystis sp.* PCC 6803 were constructed as described previously (*25*). These variants correspond to $D575K_{PsaB}$, $D575A_{PsaB}$, $D566K_{PsaB}$, $D566A_{PsaB}$, and $R570_{PsaB}$ in *Thermoynechococcus elongatus*, which is the nomenclature used in this paper. The PS I complexes used in this study were isolated from the identical batch of cells used in ref *25* after thawing from long-term storage at −80 °C. To summarize the results of ref *25*, the growth of the $D566K_{PsaB}$ variant was impaired under low light and the Chl content per cell was lower than the wild-type, but the growth and Chl content of the other four variants were identical to the wild-type. PS I complexes from all of the variants, including $D566K_{PsaB}$, showed rates of $NADP^+$ reduction no less than 75% of the wild-type, and the amplitude and kinetics of the backreaction with P_{700}^+ on a single turnover flash showed efficient electron transfer to the terminal Fe/S clusters, F_A/F_B (*25*). Thus, all of the PS I variants under study here efficiently converted light into a stable charge-separated state between P_{700} and the terminal acceptors, F_A/F_B.

Sample Preparation. For low temperature transient electron paramagnetic resonance (TR EPR) experiments 10 μL of 0.8 M sodium ascorbate (NaAsc) was added to the solution of 150 μL of sample and the sample was dark adapted and frozen in liquid nitrogen in the dark. For high temperature TR EPR experiments, 10 μL of 0.8 M NaAsc and 10 μL of 0.08 M phenazine methosulfate were added to the solution of 60 μL of sample; again the sample was dark adapted and frozen in liquid nitrogen and stored in the dark until measurement.

Time-Resolved EPR Spectroscopy. The kinetics of $A_{1A}^{\bullet-}$ oxidation were measured by transient EPR on the nanosecond time scale by monitoring the $P_{700}^{\bullet+}A_{1A}^{\bullet-}$ radical pair (RP) state. X-band transient EPR experiments at 260 K and below

were carried out using a Bruker ER046 XK-T microwave bridge equipped with a Flexline dielectric resonator (*26*) and an Oxford liquid helium gas-flow cryostat. The loaded *Q*-value for this dielectric ring resonator was about $Q = 3000$, equivalent to a rise time of $\tau_r = Q/(2\pi^*\nu_{mw}) \approx 50$ ns. The samples were illuminated using a Spectra Physics Nd:YAG/MOPO laser system operating at 10 Hz at either the second harmonic (532 nm) or near the long wavelength absorption edge of PS I at ~700 nm. Corresponding measurements at room temperature were performed using a rectangular resonator and a flat cell as described in ref *8*.

Time-Resolved Optical Spectroscopy. The fast and slow kinetic phases attributed to A_{1A}^- and A_{1B}^- oxidation were measured optically on the nanosecond time scale by monitoring flash-induced transient absorption changes at 380 nm using a time-resolved spectrophotometer similar to that described in ref *27*. The excitation beam was provided by a frequency-doubled ($\lambda = 532$ nm), Q-switched Nd:YAG laser (DCR-11, Spectra Physics, Mountain View, CA) operated in the short pulse mode (ca. 3 ns). The measuring light was provided by a xenon flash that was tailored with a bank of inductors and capacitors to produce a relatively constant light intensity for a duration of 5 μs. The 380 nm measuring beam was filtered using a combination of narrow-band (8 nm) interference and colored glass filters (to block the scattered laser flash) prior to the sample and in front of the Si photodiode detector (FND 100Q from EG&G). The photocurrent was changed to a voltage across a 50 Ω resistor, and the signal was amplified using a laboratory-built gain block (30 dB, 500 Hz to 1.7 GHz) and recorded using a digitizing oscilloscope (DSA 602A with amplifier plug-in 11A52 from Tektronix, Beaverton, OR). A photodiode connected to a 11A72 plug-in detected the laser flash and initiated the data acquisition. The rise-time of the detection system was measured using $Ru(Bipy)_3Cl_2$ luminescence to be 3 ns (*28*). The baseline was recorded after every flash by mechanically blocking the excitation flash, and the no-flash transient was subtracted from that recorded with flash excitation on every cycle. Typically, 1024 or 2048 pairs of flash minus no-flash transients were averaged at a repetition rate of 1 Hz. Software written in LabView controlled the timing sequence and the acquisition and manipulation of the data. The sample was contained in a 10 × 10 mm standard quartz cuvette. All spectroscopic measurements were performed at room temperature. Kinetic traces were analyzed by fitting with a multiexponential function using Marquardt least-squares algorithm that was programmed in IGOR Pro v. 5.2 (Wavemetrics, Lake Oswego, OR).

Data Analysis of Optical Kinetics. The number of exponential terms necessary to obtain a "good" fit of noisy (realistic) data is often arbitrary. One approach to fit the kinetics is provided by the Kohlrausch law (*29*, *30*), otherwise known as a stretched-multiexponential, in which each component is represented as $A(t) = A_0 \exp((-t/\tau)^{\beta})$, and in which the stretch parameter, β, varies between 0 and 1 (with 1 being a simple exponential). The stretch parameter provides a measure of the heterogeneity of the kinetics. Such a heterogeneity has been reported in PS I (*31*) and in reaction clusters from purple bacteria (*32*). This equation represents a robust solution of a general equation for kinetics with a distributed time constant (*33*). The advantage to a stretched exponential is that it is model-independent; the disadvantage is that it provides little insight into mechanisms or pathways. The other approach is to use a model-dependent method of fitting in which the number of exponentials is specified by a previously established number of kinetic events. Here, we accept the premise that the fast ($\tau = 7$ to 20 ns) and slow ($\tau = 150$ to 300 ns) kinetic phases are due to electron transfer through the PsaB-branch and PsaA-branch of electron transfer cofactors, respectively (*4*).

Computational Studies. For our computational study of native PS I, we used the crystal structure from *T. elongatus* at 2.5 Å resolution (PDB entry 1JB0) (*18*). The crystal structures of the PS I variants used here have not been solved. For the model of the PS I variants, only the side chain at the altered site was energetically optimized with CHARMM (*34*), keeping the positions of all non-hydrogen atoms fixed at crystallographically determined coordinates. This procedure ignores possible conformational changes of side chains of the substituted amino acids that are often accompanied by a change in net charge (e.g., as seen in the induced side chain reorientation in the proton channel near the secondary quinone in bacterial photosynthetic reaction centers (*35*−*37*)). Nevertheless, the structural models used for the PS I variants represent the best starting point for electrostatic energy computations without introducing additional uncertainties in atomic coordinates that may occur by more extensive manipulation of crystallographic atomic coordinates. Hence, for both the native and PS I variants, the atomic coordinates were treated essentially as in previous work (*19*, *38*). In the original crystal structure, atomic coordinates of PsaK were available for only the protein backbone (*18*), and in previous work we did not include this subunit (*19*, *38*). In the present study, we generated and energetically optimized side chains in the PsaK based on the CHARMM22 (*39*) parameter set. Some Chl *a* molecules in PS I possess a water molecule as a ligand. We included these water molecules in the present set of calculations. However, their influence on the midpoint potentials of A_{1A}, A_{1B}, and F_X was found to be negligible.

In the crystal structure, hydrogen atom positions were energetically optimized with CHARMM (*34*). During this procedure the positions of all non-hydrogen atoms were fixed, and all titratable groups were kept in their standard protonation state, i.e., acidic groups were ionized and basic groups were protonated. All the Chl *a* molecules except for the B-branch Chl *a* of the P_{700} dimer (P_B) and the two phylloquinones were kept in the oxidized neutral charge state. A positive unit charge was located on the P_B half of P_{700} according to ENDOR and ESEEM studies (*40*−*43*). We considered F_X, F_A, and F_B to be in the oxidized charge state $[Fe_4S_4(SCH_3)_4]^{2-}$ (*44*). All other procedures followed the description given in refs *19* and *38*. To calculate the midpoint potential of F_X, $[Fe_4S_4(SCH_3)_4]^{2-/3-}$ was considered for the oxidized/reduced states.

Using a single core processor for the calculations (e.g., an AMD Opteron operating at 1.4−1.6 GHz), the approximate CPU time required for each step of the calculations in the present study is as follows: ~1 h for the energy minimization process involving hydrogen atom geometries of the protein, ~1 week for the Poisson−Boltzmann calculation, and ~30 to 60 min for the MC sampling. Note that computation time depends not only on the performance of the hardware but also on the conditions specified in the

programs (e.g., protein size, the number of steps required for energy minimization of the hydrogen atom geometry, the number of titratable sites in the protein, and the number of grid points required for the Poisson−Boltzmann calculation).

RESULTS

1. Structural Integrity of the A_{1A} Binding Site. In PS I, two fractions of reaction centers with different electron transfer behavior are observed at low temperature, see ref *31*. In one fraction, stable charge separation occurs between P_{700} and the terminal iron sulfur clusters F_A and F_B. In the other fraction electron transfer to F_A and F_B is blocked and cyclic electron transfer takes place between P_{700} and phylloquinone. The radical ion pair $P_{700}^{\bullet+}A_{1A}^{\bullet-}$ in the latter fraction can be observed by transient EPR, and point mutation studies have shown that this radical pair involves the quinone that is located on the PsaA branch, for a review see ref *9*. The TR EPR spectrum (i.e., spin polarization pattern) of the $P_{700}^{\bullet+}A_{1A}^{\bullet-}$ state is sensitive to the orientation and spin density distribution of the quinone (see refs *9* and *45* for recent reviews). Thus, it provides a good test of the structural integrity of the A_{1A} site after a change has been introduced elsewhere in PS I. The Asp residues targeted for mutation are located sufficiently distant from A_{1A} and A_{1B} (∼9 Å or more), such that only minor alterations of the quinone binding sites are expected. This was verified by direct detection of the transient X- and Q-band spectra of the $P_{700}^{\bullet+}A_{1A}^{\bullet-}$ state for PS I trimers isolated from the D575A_{PsaB}, D575K_{PsaB}, D566A_{PsaB}, D566K_{PsaB} variants measured in frozen solution at low temperature (80 K, data are shown in Figure 1S, Supporting Information). The overall polarization patterns for both sets of variants are highly similar to the wild-type, and no significant differences in the partially resolved methyl hyperfine structure, such as were observed earlier for the W697F_{PsaA} and S692C_{PsaA} variants (*7*, *8*), are found in these spectra. Because changes in the nature of the side chains at amino acids 575_{PsaB} and 566_{PsaB} do not induce any significant alterations either in the orientation of the quinone or in the spin density distribution over the quinone ring, we conclude from the point of view of TR EPR that the integrity of the A_{1A} binding site is intact.

2. Forward Electron Transfer from A_{1A} and A_{1B} to F_X. 2.1. Analysis of A_{1A} and A_{1B} to F_X Electron Transfer by Time-Resolved Optical Spectroscopy. The resolution available in time-resolved optical absorbance difference spectroscopy provides access to electron transfer kinetics between A_{1A} and F_X and between A_{1B} and F_X limited at short times by the width of the laser actinic flash and at long times by the droop in the (lengthened) xenon measuring flash. In practice, data can be obtained in a 5 ns to 5 μs time window. Figure 2 (top) depicts typical flash-induced absorbance changes measured at 380 nm for wild-type PS I. The kinetics can be reasonably fit to a stretched exponential (Table 1), which represents a robust solution of a general equation for kinetics with a distributed time constant. The deviation in the stretch factor, β, from 1.0 indicates that the kinetics are not monoexponential, but instead, are heterogeneous. Figure 2 further depicts the results of a model-dependent method of fitting the kinetics to two discrete exponentials. A fast kinetic phase with a lifetime of ∼15 ns represents 20% of the total absorbance change, and a slow kinetic phase with a lifetime of ∼260 ns represents 80% of the total absorbance change.

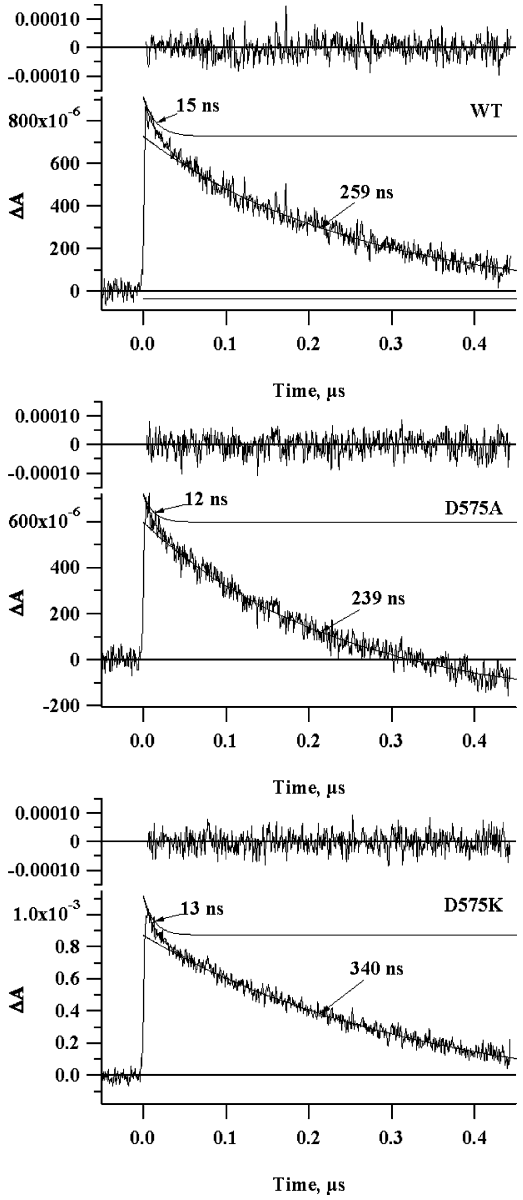

FIGURE 2: Time-resolved optical kinetics at 380 nm in the wild-type (top), and the D575A_{PsaB} (middle) and D575K_{PsaB} (bottom) variants. The ΔA_{380} kinetics are presented on a linear time scale so that the fast kinetic phase attributed to A_{1B}^- oxidation can be visualized over a broad time scale. The wild-type, D575A_{PsaB}, and D575K_{PsaB} samples were measured at 10 μg mL^{-1} Chl in 25 mM Tris, pH 8.3, 10 mM sodium ascorbate, and 500 μM DPIP. The computer-generated exponential fit is shown as a solid line. Results of the exponential fits are displayed as fit curves, where each individual component is plotted with a vertical offset relative to the next component (with a longer lifetime) or the baseline, the offset being equal to the amplitude of the latter component. The relative contributions of each kinetic phase can be judged by the intersection of the fit line with the abscissa. The residual of the fit is depicted above the main trace.

These values are similar to those reported previously for cyanobacterial PS I, and have been attributed to the oxidation of A_{1B}^- and A_{1A}^-, respectively (*4*, *7*). An indication of the precision of the measurement is provided by studies of five independently prepared wild-type samples, which show a mean lifetime and standard deviation for the fast and slow kinetic phases of 14.5 ± 5 ns and 272 ± 30 ns, respectively. The trace decays to a stable (on the nanosecond time scale) absorbance slightly below the baseline, thus representing a

Table 1: Evaluated Time Constants (k^{-1}) in ns for the Electron Transfer Kinetics A_1 to F_X at Room Temperature (295 K) and 260 K[a]

	TR EPR k^{-1} (ns)		time-resolved optical spectroscopy: stretched exponential fit		time-resolved optical spectroscopy: double exponential fit		
			k^{-1} (ns)	stretch factor (β)	slow phase k^{-1} (ns)	fast phase k^{-1} (ns)	fast phase rel amplitude (%)
WT^{295K}	280		239	0.86	259	15	20
$D575A_{PsaB}$	320	360*	232	0.81	239	12	13
$D575K_{PsaB}$	340	410*	371	0.73	340	13	20
$D566A_{PsaB}$		245*	116	0.79	149	10	20
$D566K_{PsaB}$		210*	106	0.74	122	10	20
$R570E_{PsaB}$			222	0.81	255	20	22
WT^{260K}	785						
$D575A_{PsaB}$	1070						
$D575K_{PsaB}$	1280						
$D566A_{PsaB}$	685						
$D566K_{PsaB}$	590						

[a] The time constants are evaluated from EPR data by fitting an appropriate model function of time to the experimental transients as described in the text. The optical transients were fitted with either a stretched exponential or biexponential decay function as described in the text. Time constants marked by * are not measured but extrapolated using the Arrhenius plots shown in Figure 1S (Supporting Information). The activation energy of wild type was set to 220 ± 20 meV (see ref *31*). From the limited data set at four temperatures between 290 and 260 K the activation energies are evaluated to 245 and 255 meV, for the variants $D575A_{PsaB}$ and $D575K_{PsaB}$, respectively. Within the larger error margins these values do not differ from the wild type value of 220 ± 20 meV. The latter has been taken for extrapolation of the data for the $D566A_{PsaB}$ and $D566K_{PsaB}$ variants.

net bleaching, and it returns back to the baseline with a lifetime of 30 μs (data not shown). The decay-associated spectrum of the bleaching from 360 to 520 nm is characteristic of a Chl triplet (data not shown). Because this triplet is most probably generated by intersystem crossing in the antenna Chls, and is generated on the order of subnanoseconds, its rise and subsequent decay are not expected to compromise the analysis of the kinetics of the fast and slow phases of quinone oxidation.

In general, the lifetimes and amplitudes of the slow and fast kinetic phases of the four PS I variants do not differ significantly (i.e., more than a factor of 2) from the wild-type. The kinetics of the $D575A_{PasB}$ and $D575K_{PsaB}$ variants can be similarly fitted to a stretched exponential (Table 1) and to a model dependent fitting to two exponentials. The lifetime of the slow kinetic phase in the $D575A_{PasB}$ variant (Figure 2, middle) is similar to the wild-type, while the lifetime of the slow kinetic phase in the $D575K_{PsaB}$ variant (Figure 2, bottom) is somewhat longer than the wild-type. The kinetics of the $D566A_{PasB}$ and $D566K_{PsaB}$ variants can be similarly fit to a stretched exponential (Table 1) and to a model dependent fitting to two exponentials. The lifetimes of the slow kinetic phase in the $D566A_{PasB}$ (Figure 3, top) and $D566K_{PsaB}$ (Figure 3, middle) variants are somewhat shorter than for the wild-type. In all four variants, the ratio of the fast to the slow kinetic phase is similar to the wild-type (Table 1). Although the lifetime of the fast phase in the $D566A_{PasB}$ and $D566K_{PsaB}$ variants appears shorter than in the wild-type and the $D575A_{PasB}$ and $D575K_{PsaB}$ variants (Figures 2 and 3), the low amplitude of the fast kinetic phase and the relatively low number of data points make it difficult

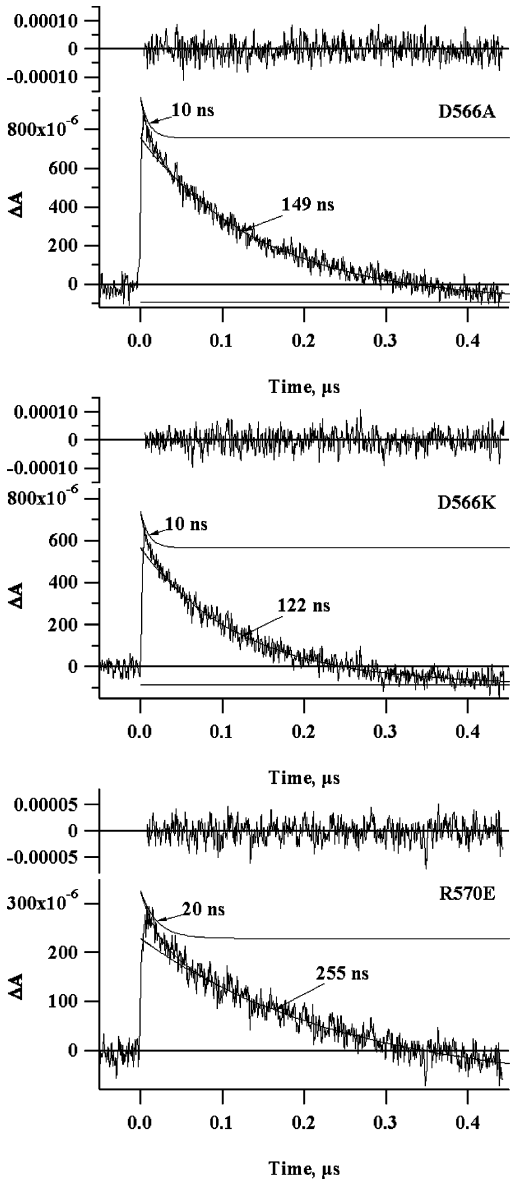

FIGURE 3: Time-resolved optical kinetics at 380 nm in the $D566A_{PsaB}$ (top), $D566K_{PsaB}$ (middle), and E570D (bottom) variants. The $D566A_{PsaB}$, $D566K_{PsaB}$, and $E570K_{PsaB}$ samples were measured at 11 μg mL^{-1} Chl *a*, 10 μg mL^{-1} Chl *a*, and 8 μg mL^{-1} Chl *a*, respectively, in 25 mM Tris, pH 8.3, 10 mM sodium ascorbate, and 500 μM DPIP. See Figure 3 for further details.

to draw firm conclusions about changes in lifetime except that they are not significantly altered. The $R570E_{PsaB}$ variant was employed as a control because the charged side group is relatively distant from both F_X and A_{1A}/A_{1B} and because the change from Arg to Glu does not uncover an uncompensated charge. As expected, the lifetime and the stretch factor of the stretched exponential fit (Table 1), and the lifetimes and amplitudes of the fast and slow kinetic phases of the two-exponential fit (Figure 3, bottom), are similar to the wild-type.

2.2. Analysis of A_{1A} to F_X Electron Transfer by Transient EPR Spectroscopy. The kinetics of the slow phase of electron transfer from A_{1A} to F_X can also be followed by transient EPR spectroscopy. In this case the accessible time region is limited at short times to ~50 ns mainly by the bandwidth of the resonator and at long times by the decay of the spin polarization due to spin−lattice relaxation. Figure 4 presents

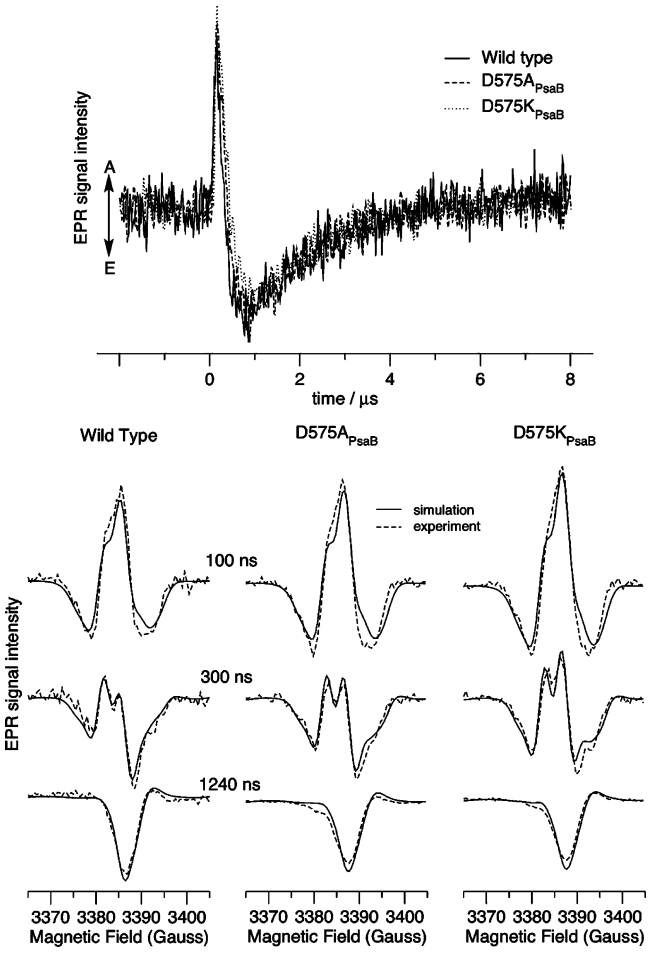

FIGURE 4: Top: Selected room temperature EPR transients from the wild type (solid trace) and the D575A$_{PsaB}$ (dashed trace) and D575K$_{PsaB}$ (dotted trace) variants. The field position at which the transients were taken has been selected so that the contribution from $P_{700}^{\bullet+}A_1^{\bullet-}$ is absorptive (positive) while $P_{700}^{\bullet+}F_X^{\bullet-}$ gives an emissive (negative) signal. Bottom: Room temperature spin polarized EPR spectra taken at three different delay times for wild type PS I (left) and the D575A$_{PsaB}$ (middle) and D575K$_{PsaB}$ (right) variants. The dashed curves are the experimental data, and the solid curves are corresponding spectra taken from a simulation of the entire time/field datasets.

TR EPR measurements at room temperature from wild type PS I and the two 575$_{PsaB}$ variants. The top part of Figure 4 shows selected transients taken at a field position near the middle of the series of spectra shown in the lower part of Figure 4 for three different time delays after the laser flash. The transients show a change from an absorptive (positive) signal at early time to an emissive (negative) signal at later time as the electron is transferred from A_{1A}^- to the Fe/S cluster, F_X. In the spectra, the electron transfer leads to a change from an E/A/E polarization pattern at early time to a primarily emissive pattern at late time. Consistent with the optical data, the transient EPR results in Figure 4 show little difference between the variants and the wild type. However, closer examination of the spectra at 300 ns after the laser flash reveals subtle differences in the patterns. In this time window, the polarization patterns from all three samples are a nearly equal mixture of the E/A/E pattern due to $P_{700}^{\bullet+}A_{1A}^{\bullet-}$ and the emissive pattern due to $P_{700}^{\bullet+}F_X^{\bullet-}$. These spectra are very sensitive to the electron transfer lifetime because changes in the lifetime alter the admixture of the two spectra. Inspection of the spectra at 300 ns shows that the emissive contribution is strongest in the wild type and weakest in the D575K$_{PsaB}$ variant. This difference suggests that the rate of electron transfer is indeed slowed in the two variants and is slowest in the Lys variant. The slight change in the electron transfer rate is also revealed by simulations of the time/field datasets in which the electron transfer lifetime was fitted to the experimental data as described (*26*). The results of the fits are shown as solid curves in the lower part of Figure 4, and the lifetimes obtained are 280 ns (wild type), 320 ns (D575A$_{PsaB}$), and 340 ns (D575K$_{PsaB}$).

These differences become more apparent when electron transfer is slowed down at lower temperatures. Corresponding data at 260 K for the D575$_{PsaB}$ and D566$_{PsaB}$ variants are shown in Figure 5 top and bottom, respectively. On the right of Figure 5, transients are shown taken at selected field positions indicated by arrows under the spectra on the left. At field position a, only the $A_{1A}^{\bullet-}$ contribution to the $P_{700}^{\bullet+}A_{1A}^{\bullet-}$ RP spectrum is observed, so that the decay of the TR EPR signal at this field position represents mainly the forward electron transfer rate, provided that it is significantly faster than the decay of the spin polarization. At other field positions, contributions from both of the intermediate RP states $P_{700}^{\bullet+}A_1^{\bullet-}$ and $P_{700}^{\bullet+}(Fe/S)^{\bullet-}$ are observed. The slowing of the A_{1A}^- to F_X electron transfer in the D575$_{PsaB}$ variants is seen most clearly in the transients at field position b. It is apparent that the Lys variant (dotted curve) shows a larger effect than the Ala variant (dashed curve). In contrast, alteration of D566$_{PasB}$ (Figure 5, bottom) leads to the opposite effect: the A_{1A} to F_X electron transfer in the D556A$_{PsaB}$ and D556K$_{PsaB}$ variants is faster than in the wild-type. Again, the Lys variant shows a larger effect than does Ala. The electron transfer lifetimes obtained by fitting the TR EPR data, together with an extrapolation of data at three different lower temperatures to room temperature (295 K), are collected in Table 1.

Electron transfer from A_{1A}^- to F_X is known to be thermally activated and shows Arrhenius behavior with an activation energy evaluated to 220 ± 20 meV in *T. elongatus* (*31*). This value, together with the Marcus equation for the activation energy suggests that the reorganization energy, λ, is much larger than the driving energy, ΔG (*31*). Under these conditions, Marcus theory predicts that the activation energy remains nearly unaffected as the ΔG varies. This is verified with kinetic results for the two D575$_{PasB}$ variants at different temperatures, see Figure 2S (Supporting Information). Within the uncertainty of the data, no significant change is observed in the activation energy. The changes in driving energy $\Delta\Delta G$ can also be estimated from the data. Using a reorganization energy λ between 0.8 and 1.1 eV and an electronic coupling value of 1.12 eV (*31*), the experimental electron transfer rates at 260 K correspond to a very small shift of $\Delta\Delta G \approx -20$ meV in the driving energy for each of the D575$_{PsaB}$ variants, and a shift of similar magnitude, but opposite sign for the D566$_{PsaB}$ variants.

DISCUSSION

The results of the electron transfer kinetic studies of the Ala and Lys variants of D575$_{PsaB}$ and D566$_{PsaB}$ can be summarized as follows: (i) In both sets of variants only small changes of less than a factor of 2 in the A_{1A} and A_{1B} to F_X electron transfer rates are observed. (ii) There are systematic

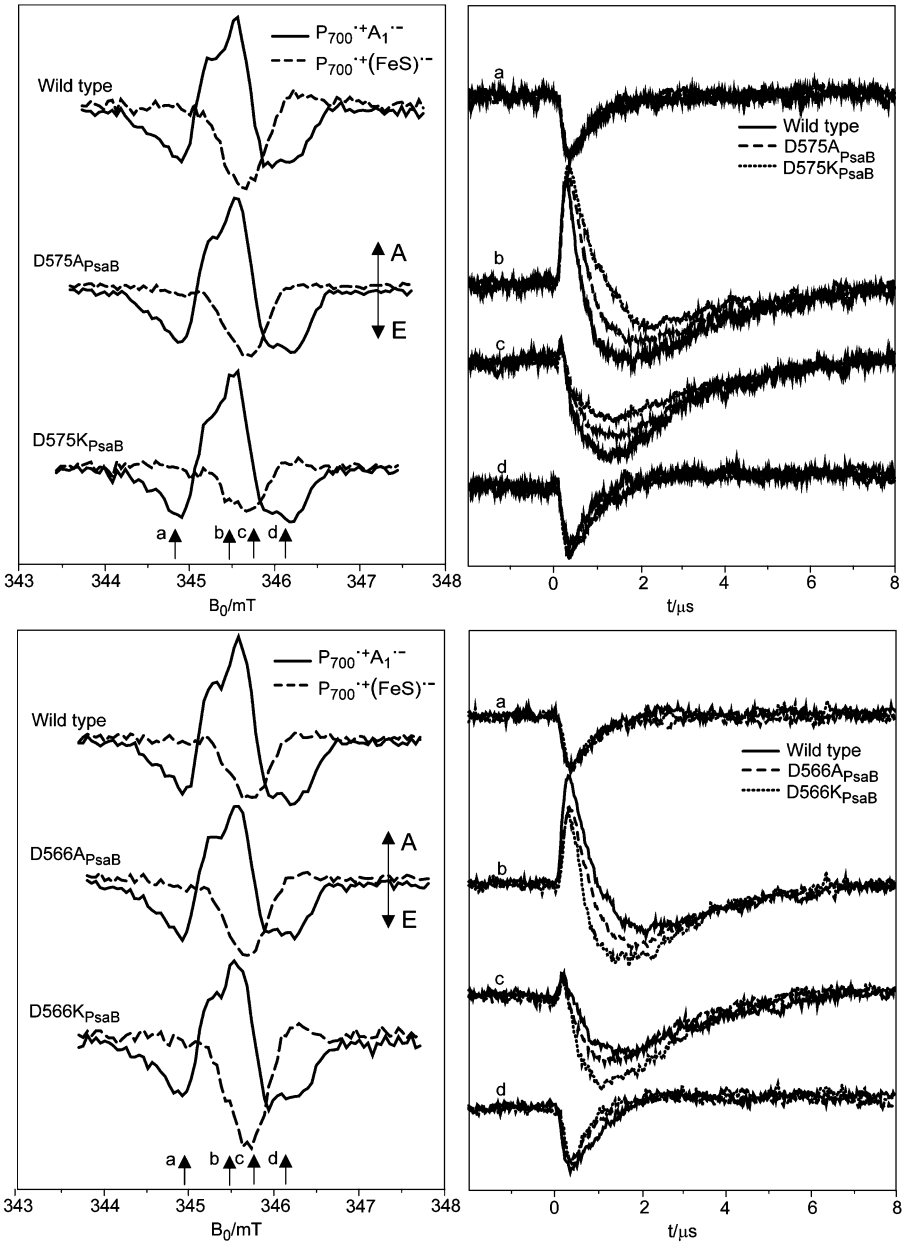

FIGURE 5: Comparison of transient spin polarized EPR data at 260 K with electron transfer observable between consecutive radical ion pair intermediates assigned to the $P_{700}^{\bullet+}A_1^{\bullet-}$ and $P_{700}^{\bullet+}F_X^{\bullet-}$ RP states. The microwave field was attenuated by 30 dB in order to suppress transient nutations modulating the observed transients. Top, left: Transient spectra at early time (solid curves, time window 200−400 ns) and at late time (dashed curves, 1.75−2.25 μs) for wild type PS I (top) and the D575A$_{PsaB}$ (middle) and D575K$_{PsaB}$ (bottom) variants. Top, right: TR EPR kinetic traces (transients) from the same data set at selected field positions, as indicated by the arrows labeled a−d below the spectra in the left part. From the transients the electron transfer time constants are evaluated to 785 ns, 1070 ns, and 1280 ns for the wild type, D575A$_{PsaB}$, and D575K$_{PsaB}$ PS I particles, respectively. Bottom: Corresponding set of data, but for PS I trimers from the wild type and the variants D566A$_{PsaB}$ and D566K$_{PsaB}$. Bottom, left: TR EPR spectra at early time (solid curves, 200−450 ns) and late time (dashed curves, 1.5−2 μs, 1.75−2.25 μs for wild type). Bottom, right: Transients at selected field positions. The electron transfer time constants are evaluated to 785, 685, and 590 ns for PS I for wild type, D566A$_{PsaB}$, and D566K$_{PsaB}$, respectively.

trends in the kinetics such that introducing Lys generally causes a larger effect than introducing Ala. (iii) Alteration of D575$_{PsaB}$ in the vicinity of A_{1A} decreases the electron transfer rate while alteration of D566$_{PsaB}$ in the vicinity of F_X increases it, consistent with an opposite change of the driving force of the A_{1A} to F_X electron transfer process for the two variants. (iv) The decrease in the electron transfer rate induced by alteration of D575$_{PsaB}$ is less than that observed when residues in more intimate contact with the quinone are altered, e.g., W696$_{PsaA}$, which is π-stacked with the quinone; and S692$_{PsaA}$, which is connected by H-bonds to W696$_{PsaA}$ and R694$_{PsaA}$ as part of an H-bond network that spans from A_0 to F_X (*15*, *16*). Qualitatively, the effect on the electron transfer rate for the two sets of variants can be rationalized in terms of the expected changes to the electrostatic environment in the vicinity of A_{1A}, A_{1B}, and F_X. The partial negative charge associated with the side chain of D575$_{PsaB}$ is predicted by electrostatic calculations to play a prominent role in establishing the very negative midpoint potentials of A_{1A}, A_{1B}, and F_X (*19*). Removing this negative charge by replacing D575$_{PsaB}$ with a neutral residue such as Ala should drive the midpoint potentials of A_{1A} and A_{1B} more

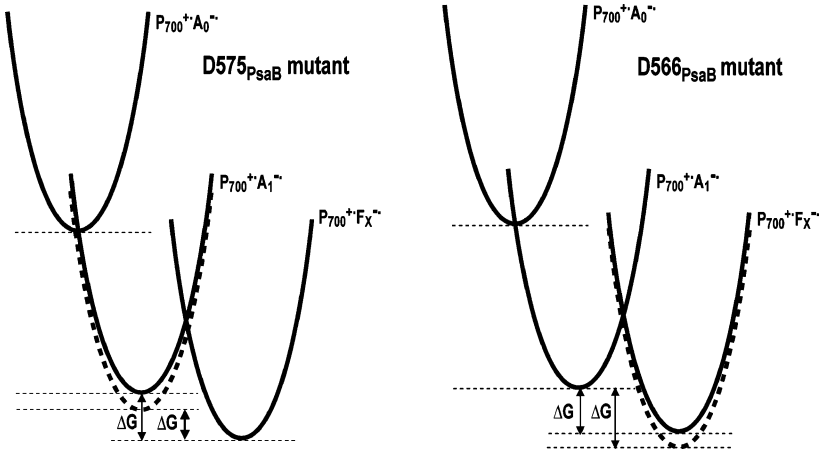

FIGURE 6: The scheme of parabolic midpoint potential curves along the reaction coordinate (according to Marcus theory) is used to illustrate the predominant downward shift in the potential due to the Asp mutation to Ala or Lys. Left: The D575$_{PsaB}$ variant affects predominantly the A_1 potential; for simplicity only its downward shift is indicated. Right: The D566$_{PsaB}$ variant affects predominantly on the F_X midpoint potential; for simplicity only its downward shift is indicated. Note that the respective shifts lead to opposite changes of the midpoint potential difference ΔG between A_1 and F_X, and therefore to opposite changes of the driving energy for the A_1 to F_X electron transfer, in agreement with the experimentally observed changes in the electron transfer rate.

positive, and this effect should be more pronounced when a positively charged residue such as Lys is introduced. Alteration of D566$_{PsaB}$, on the other hand, disrupts the salt bridge it forms to PsaC. Removal of this bridge would be expected to expose positive charges and drive the midpoint potentials of A_1 and F_X more positive, and again a larger effect is expected for the Lys variant because of its positively charged side chain. Thus, similar changes to the electrostatic environment are expected in both sets of variants. However, the location of the residue being changed plays a decisive role in determining how the kinetics are altered. In the D575$_{PsaB}$ variants it is presumed that the potential of A_{1A} is predominantly driven more positive and hence the driving energy is reduced and the A_{1A} to F_X electron transfer is slowed. In the D566$_{PsaB}$ variants, it is presumed that the potential of F_X is predominantly driven more positive and this increases the driving energy and the electron transfer rate. Figure 6 illustrates the effect of a positive shift in midpoint potential and the consequence of opposite changes in the driving energy and the electron transfer rates depending on which species is shifted more strongly.

The result is that the ~20 meV change in the driving energy is surprisingly small, particularly when compared with the ~200 meV contribution of the negative charge that D575$_{PsaB}$ is predicted to make to the midpoint potential of A_{1A} when D575$_{PsaB}$ is fully ionized (*19*, *20*). To understand why such small changes in the electron transfer rates are observed, we have extended our computational studies to include the shifts in midpoint potential of F_X as well as of A_{1A} and A_{1B}. The values listed in Table 2 indicate the following features: (a) With the loss of the negative charge on D575$_{PsaB}$ (alternately, the appearance of an uncompensated positive charge) significant upward shifts in the midpoint potential are calculated for the quinones and Fe/S cluster. For the D575$_{PsaB}$ variants, these shifts are rather similar for A_{1A}, A_{1B}, and F_X. Hence, the A_{1A}/F_X and the A_{1B}/F_X *differences* in midpoint potential from the wild-type ($\Delta\Delta E$) are small, and this is in agreement with the experimentally observed small effects on the A_{1A} to F_X and the A_{1B} to F_X electron transfer rates. For the D575$_{PsaB}$ variants, the calculated upward shifts turn out to be slightly larger for F_X than for A_{1A} and even more so for the D566$_{PsaB}$ variants, while the experimental results indicate the opposite trend. In addition, the calculated shifts are not significantly different for the Ala and Lys variants (they cannot be if only because the side chain (Asp) at the altered site was energetically optimized while the coordinates of all non-hydrogen atoms are kept fixed). However, the experimental results indicate a small but systematic difference on top of the opposite sign for the D575$_{PsaB}$ and D566$_{PsaB}$ variants. This discrepancy may indicate a role of the charged state of the varied side chain. Moreover, the replacement of D575$_{PsaB}$ with Lys, and to some extent also with Ala, may lead to a conformational change that is often accompanied by an alteration in the character of the charged residue (*35*−*37*). Note that the replacement of uncharged residues may also lead to a slight rearrangement of side chains as shown in flavodoxin from *Clostridium beijerinckii* (*46*). These conformational changes have been shown to play a role in controlling the midpoint potentials in flavodoxin (*46*) and in rubredoxin from *Clostridium pasteurianum* (*47*). Crystallographic studies of the V44 mutants of rubredoxin indicate that the size of the side chain plays an important role in tuning the midpoint potential (H. Ishikita, unpublished). (b) For the D566$_{PsaB}$ variants a significant upward shift in midpoint potential is only calculated for F_X, while for the A_{1A} and A_{1B}, the changes are marginal. Correspondingly, the driving energy for A_{1A} and A_{1B} to F_X electron transfer is predicted to increase. Indeed, the A_{1A} to F_X electron transfer rates were observed

Table 2: Calculated Shifts (ΔE_m) in the Midpoint Potential (E_m) in mV and Driving Energy for the $A_1 \rightarrow F_X$ Electron Transfer ($\Delta(\Delta E)$) in meV Relative to the Wild Type E_m in mV

	ΔE_m[a]			$\Delta(\Delta E)$[a]	
	A_{1A}	A_{1B}	F_X	$A_{1A} \rightarrow F_X$	$A_{1B} \rightarrow F_X$
D575A$_{PsaB}$	+119	+136	+123	−4	+13
D575K$_{PsaB}$	+125	+144	+132	−7	+12
D566A$_{PsaB}$	−19	+8	+53	−72	−45
D566K$_{PsaB}$	−20	+8	+54	−74	−46

[a] Calculated values with the native crystal structure for the native PS I complex from *T. elongatus* (*18*). For the mutant PS I complex, model structures were used (see Materials and Methods).

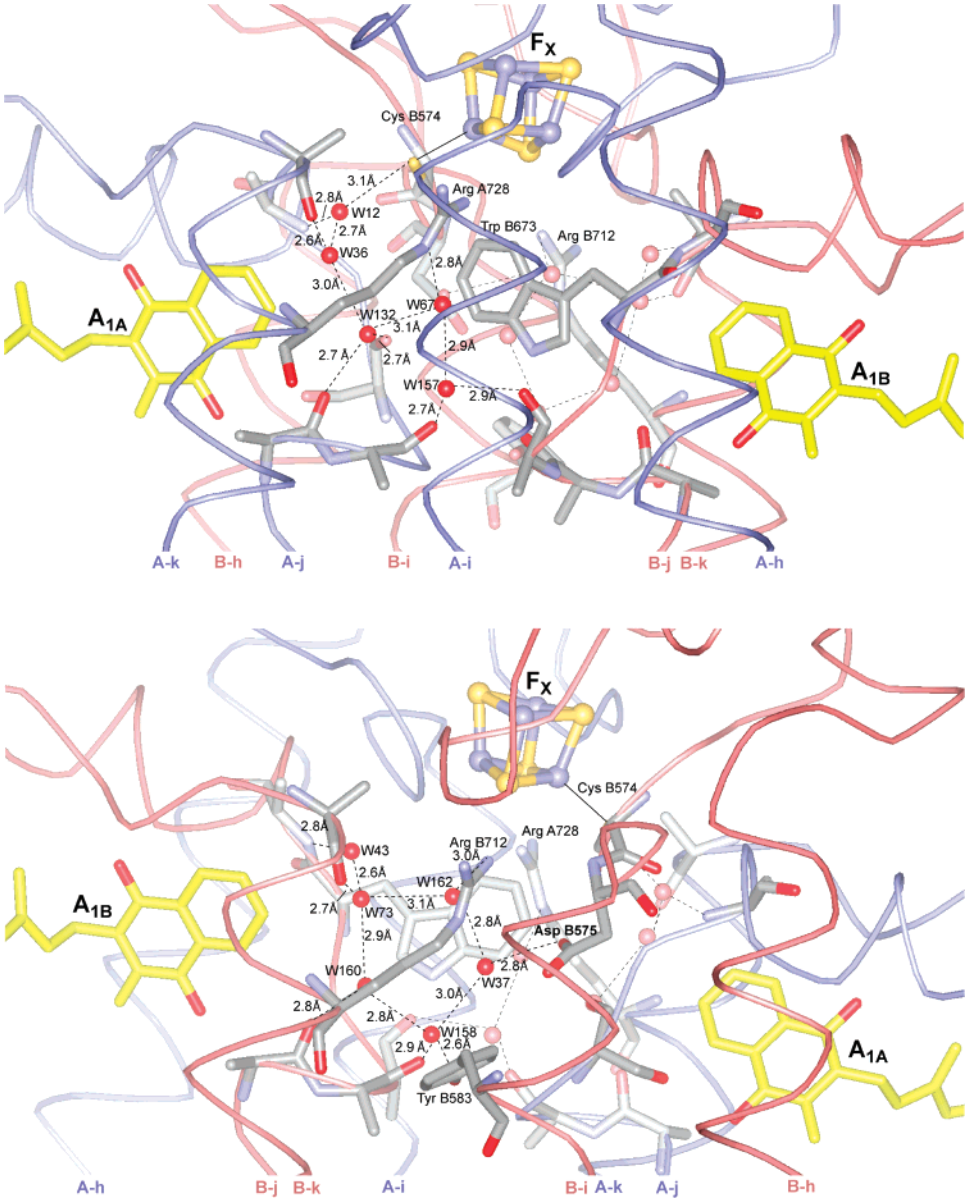

FIGURE 7: Detail of the structural model of PS I (PDB entry: 1JB0) in the vicinity of the acceptors A_{1A}, A_{1B}, and F_X. The view projection is approximately parallel to the membrane surface and onto a plane passing through the centers of the acceptors. The structure is viewed from opposite directions in the top and bottom parts of the figure. Note the two inequivalent networks of bound water molecules located between the quinones and first Fe/S center F_X as described in the text. Possible H-bonds between the water molecules and the backbone and/or side chains of amino acids in the protein environment are indicated by thin lines. While the PsaA-side bound water network has 5 members in an approximately linear arrangement, the PsaB-side one has 6 members of which five are arranged in a pentagon arrangement. Note that a crucial H-bond to W-37 is provided in this case by the B-side specific $D575_{PsaB}$ side chain.

to increase (the A_{1B} to F_X electron transfer rate also appeared to increase, but the low amplitude of the fast kinetic phase restricts our confidence in the measurement). However, again the difference between the $D566A_{PsaB}$ and $D566K_{PsaB}$ variants is negligible compared to the experiment, probably for the same reason as mentioned above. Note that the change in the calculated driving energy is higher for the PsaA- than the PsaB-side (almost double for the PsaA-side). Indeed $D566_{PsaB}$ is located closer to A_{1A} than A_{1B} although it is much closer to F_X. (c) The calculated driving energy for A_{1A} to F_X electron transfer is increased for the $D566_{PsaB}$ variants but remains nearly unchanged for the $D575_{PsaB}$ variants. Experimentally, the change is of opposite sign for the two variants with nearly equal absolute value. Recall that the changes are small in any event, and a slight change in the absolute values of the driving energy would put calculated and observed changes in agreement.

The calculated values of midpoint potentials are relatively independent of the electron spin distribution on P_{700}. In the present calculations, we assumed that a positive unit charge was located on the P_B half of P_{700} (e.g., according to ENDOR and ESEEM studies) (*40*, *42*, *48*). In contrast, FTIR studies imply that the positive charge in P_{700}^+ is shared approximately equally between the two chlorophylls (*49*, *50*). We therefore evaluated the influence of the P_{700} charge distribution pattern on in calculated midpoint potentials for A_{1A}, A_{1B}, and F_X. In wild type PS I, the $P_A^{0.5+}P_B^{0.5+}$ charge state of P_{700} increases the computed midpoint potentials for A_{1A} and A_{1B} of 4 mV and 6 mV, respectively, with respect to the values calculated for the $P_A^0P_B^+$ charge state. On

Table 3: Two Sets of Bound Water Networks Connected to the PsaA and PsaB Subunits of PsaA/PsaB Heterodimer

subunits	water molecule	distance (Å)	type[a]	amino residue or water molecule
PsaA	W-12	3.1	S	S^{γ} Cys B574
		2.8	B	N Arg A694
		2.7	I	W36
PsaA	W-36	2.6	B	O Ile A724
		2.7	I	W12
		3.0	I	W132
PsaA	W-67	2.8	S	N^{ϵ} Arg A728
		3.1	I	W132
		2.9	I	W157
PsaA	W-132	2.7	B	O Phe A689
		2.7	B	O Ser A692
		3.0	I	W36
		3.1	I	W67
PsaA	W-157	2.7	B	O Leu A690
		2.9	B	O Ile B671
		2.9	I	W67
PsaB	W-37	2.8	S	$O^{\delta 1}$ Asp B575
		3.0	I	W158
		2.8	I	W162
PsaB	W-43	2.8	S	N Arg B674
		2.6	I	W73
PsaB	W-73	2.7	B	O Ile B708
		2.9	I	W160
		3.1	I	W162
PsaB	W-158	2.9	B	O Leu B670
		2.6	B	O^{η} Tyr B583
		3.0	I	W37
		2.8	I	W160
PsaB	W-160	2.8	B	O Phe B669
		2.9	I	W73
			I	
		2.8		W158
PsaB	W-162	3.0	S	$N^{\eta 1}$ Arg B712
		2.8	I	W37
		3.1	I	W73

[a] S: H-bond to side chain of amino residue. B: H-bond to back bone of amino residue. I: intramolecular H-bond.

similarly changing the P_{700} charge distribution pattern, the calculated midpoint potential for F_X remains unchanged. Hence, the positive charge distribution pattern in P_{700}^{+} has little effect on the calculated driving energy for A_{1A} to F_X or A_{1B} to F_X electron transfer.

In comparing the calculations with the experimental observations it is important to consider other possible structural changes that might occur in the variants and their effect on the calculated midpoint potentials. The shifts in these potentials given in refs *19* and *20* and in Table 2 depend critically on the fact that the side chain of $D575_{PsaB}$ is H-bonded directly with a water molecule (W-37), see Figure 7. This bound water is also part of a larger water network, located on the PsaB side of the complex between A_{1B} and F_X. There is a corresponding network of water molecules on the PsaA side located between A_{1A} and F_X but the number and arrangement of the water molecules in the two networks are different, see Figure 7 (both networks are tabulated in Table 3). The network on the PsaA side is composed of five water molecules in a roughly linear arrangement, while on the PsaB side five of six waters are interconnected in a pentagonal arrangement. Previous electrostatic calculations (*19*) have shown that the midpoint potentials for the quinones are influenced strongly by these water molecules and that these potentials vary significantly if no water molecules, only W-37, or all bound waters are included. The three cases yielded midpoint potentials for A_{1A} of −438, −531, and −629 mV and for A_{1B} of −604, −686, and −776 mV. These significant shifts due to the bound water molecules for the individual midpoint potential values of A_{1A}, A_{1B}, and F_X are also reflected in the respective A_{1A}/A_{1B} asymmetry ($\Delta_{A/B}$: −166, −155, and −147 mV). Accordingly, the driving energy for the A_{1A} and A_{1B} to F_X electron transfer processes may depend on the details of the bound water networks. Replacement of $D575_{PsaB}$ with either an Ala or Lys would remove the H-bond between W-37 and this residue, which would probably cause a change in the B-side water network. Inspection of the structure in Figure 7 suggests that a possible outcome of the loss of this H-bond would be a repositioning of W-37 with the possible formation of new hydrogen bonds, e.g., to the side chain of $R712_{PsaB}$ and to another bound water molecule. As a consequence of these rearrangements, water molecule W-160 would likely be lost. Without W-160 and with W-37 repositioned, the water networks on both sides would become essentially the same. Therefore alteration of $D575_{PsaB}$ would be expected to modify various electrostatic contributions to the midpoint potential of A_{1A}, A_{1B}, and F_X, in particular that of the bound water networks. Ideally, electrostatic calculations of midpoint potential shifts in $D575_{PsaB}$ variants should be based on their X-ray crystal structures. However, in the absence of such data as a starting point for the electrostatic calculations one could substitute the five-membered water network of the PsaA-side onto the B-side before calculating energy-minimized structures. A comprehensive analysis of the influence of the bound water networks in electrostatic calculations is in progress for a forthcoming publication.

In conclusion, only minor but systematic shifts in the midpoint potential difference between A_{1A} and F_X and between A_{1B} and F_X are observed in the $D575_{PsaB}$ variants studied here. This appears to occur because the contributions of $D575_{PsaB}$ to the midpoint potentials of both quinones and F_X are similar. It is also possible that the change in the identity of the side chain is compensated for by a rearrangement in the coordinates and protonation pattern of the protein environment. Another issue is that, because of the relatively long side chain of the Lys variants, modeling of atomic coordinates of the Lys mutants is uncertain. With the atomic coordinates used for the calculations of the midpoint potential, the introduced Lys residue is largely protonated, and this may have an influence on H-bonding interactions with the surroundings. To obtain the coordinates, we placed the generated Lys side chain as well as possible in the volume vacant after removal of the wild-type Asp in the original crystal structure to minimize steric hindrance. Nevertheless, in the $D575K_{PsaB}$ variant the formation of a salt-bridge between $K575_{PsaB}$ and $D580_{PsaB}$ might occur and in the case of the $D566K_{PsaB}$ variant the side chain is within H-bonding distance from $R65_{PsaC}$ and $R570_{PsaB}$. More complete sampling of the conformation space combined with variation of the degree of protonation might improve the quality of the calculated structure. However, these subtle details will be very difficult, if not impossible, to predict in the calculations without an atomic resolution X-ray crystal structure of the variant(s). The fact that the experimentally observed changes in the Asp variants are very small is not really unexpected, as the protein environment has the ability to accommodate to a large extent alterations caused by a site-directed change.

On the other hand, it is satisfying that the experimentally observed shifts, although small, are nevertheless significant and have the magnitude and sign expected from simple assumptions.

ACKNOWLEDGMENT

The authors thank Dr. Gaozhong Shen for valuable advice.

SUPPORTING INFORMATION AVAILABLE

Figure 1S (comparison of spin-polarized TR EPR spectra at X- and Q-band for the $P_{700}^{\bullet+}A_1^{\bullet-}$ state of PS I trimers in frozen solution at 80 K) and Figure 2S (Arrhenius behavior of electron transfer from A_{1A}^- to F_X in the wild-type, $D575A_{PsaB}$ and $D575K_{PsaB}$ variants). This material is available free of charge via the Internet at http://pubs.acs.org.

REFERENCES

1. Golbeck, J. (2006) *Photosystem I: The Light-Driven Plastocyanin: Ferredoxin Oxidoreductase*, Vol. 24, Springer, Dordrecht.
2. Joliot, P., and Joliot, A. (1999) *In vivo* analysis of the electron transfer within Photosystem I: are the two phylloquinones involved?, *Biochemistry 38*, 11130−11136.
3. Guergova-Kuras, M., Boudreaux, B., Joliot, A., Joliot, P., and Redding, K. (2001) Evidence for two active branches for electron transfer in Photosystem I, *Proc. Natl. Acad. Sci. U.S.A. 98*, 4437−4442.
4. Bautista, J. A., Rappaport, F., Guergova-Kuras, M., Cohen, R. O., Golbeck, J. H., Wang, J. Y., Beal, D., and Diner, B. A. (2005) Biochemical and biophysical characterization of Photosystem I from phytoene desaturase and zeta-carotene desaturase deletion mutants of *Synechocystis* sp. PCC 6803: evidence for PsaA- and PsaB-side electron transport in cyanobacteria, *J. Biol. Chem. 280*, 20030−20041.
5. Cohen, R. O., Shen, G., Golbeck, J. H., Xu, W., Chitnis, P. R., Valieva, A. I., van der Est, A., Pushkar, Y., and Stehlik, D. (2004) Evidence for asymmetric electron transfer in cyanobacterial Photosystem I: analysis of a methionine-to-leucine mutation of the ligand to the primary electron acceptor A_0, *Biochemistry 43*, 4741−4754.
6. Dashdorj, N., Xu, W., Cohen, R. O., Golbeck, J. H., and Savikhin, S. (2005) Asymmetric electron transfer in cyanobacterial Photosystem I: charge separation and secondary electron transfer dynamics of mutations near the primary electron acceptor A_0, *Biophys. J. 88*, 1238−1249.
7. Xu, W., Chitnis, P. R., Valieva, A., van der Est, A., Brettel, K., Guergova-Kuras, M., Pushkar, Y. N., Zech, S. G., Stehlik, D., Shen, G., Zybailov, B., and Golbeck, J. H. (2003) Electron transfer in cyanobacterial Photosystem I: II. Determination of forward electron transfer rates of site-directed mutants in a putative electron transfer pathway from A_0 through A_1 to F_X, *J. Biol. Chem. 278*, 27876−27887.
8. Xu, W., Chitnis, P., Valieva, A., van der Est, A., Pushkar, Y. N., Krzystyniak, M., Teutloff, C., Zech, S. G., Bittl, R., Stehlik, D., Zybailov, B., Shen, G., and Golbeck, J. H. (2003) Electron transfer in cyanobacterial Photosystem I: I. Physiological and spectroscopic characterization of site-directed mutants in a putative electron transfer pathway from A_0 through A_1 to F_X, *J. Biol. Chem. 278*, 27864−27875.
9. Stehlik, D. (2006) Transient EPR Spectroscopy as Applied to Light-Induced Functional Intermediates along the Electron Transfer Pathway in Photosystem I, in *Photosystem I: The Light-Driven Plastocyanin:Ferredoxin Oxidoreductase* (Golbeck, J., Ed.) pp 361−386, Springer, Dordrecht.
10. Semenov, A. Y., Vassiliev, I. R., van der Est, A., Mamedov, M. D., Zybailov, B., Shen, G., Stehlik, D., Diner, B. A., Chitnis, P. R., and Golbeck, J. H. (2000) Recruitment of a foreign quinone into the A_1 site of Photosystem I. Altered kinetics of electron transfer in phylloquinone biosynthetic pathway mutants studied by time-resolved optical, EPR, and electrometric techniques, *J. Biol. Chem. 275*, 23429−23438.
11. Vos, M. H., and Van Gorkom, H. J. (1988) Thermodynamics of electron transport in Photosystem I studied by electric field-stimulated charge recombination, *Biochim. Biophys. Acta 934*, 293−302.
12. Marcus, R. A. (2006) Summarizing lecture: factors influencing enzymatic H-transfers, analysis of nuclear tunnelling isotope effects and thermodynamic versus specific effects, *Philos. Trans. R. Soc. London, Ser. B 361*, 1445−1455.
13. Moser, C. C., Keske, J. M., Warncke, K., Farid, R. S., and Dutton, P. L. (1992) Nature of biological electron transfer, *Nature 355*, 796−802.
14. Moser, C. C., Page, C. C., Farid, R., and Dutton, P. L. (1995) Biological electron transfer, *J. Bioenerg. Biomembr. 27*, 263−274.
15. Boudreaux, B., MacMillan, F., Teutloff, C., Agalarov, R., Gu, F., Grimaldi, S., Bittl, R., Brettel, K., and Redding, K. (2001) Mutations in both sides of the Photosystem I reaction center identify the phylloquinone observed by electron paramagnetic resonance spectroscopy, *J. Biol. Chem. 276*, 37299−37306.
16. Fairclough, W. V., Forsyth, A., Evans, M. C., Rigby, S. E., Purton, S., and Heathcote, P. (2003) Bidirectional electron transfer in Photosystem I: electron transfer on the PsaA side is not essential for phototrophic growth in *Chlamydomonas*, *Biochim. Biophys. Acta 1606*, 43−55.
17. Purton, S., Stevens, D. R., Muhiuddin, I. P., Evans, M. C., Carter, S., Rigby, S. E., and Heathcote, P. (2001) Site-directed mutagenesis of PsaA residue W693 affects phylloquinone binding and function in the Photosystem I reaction center of *Chlamydomonas reinhardtii*, *Biochemistry 40*, 2167−2175.
18. Jordan, P., Fromme, P., Witt, H. T., Klukas, O., Saenger, W., and Krauss, N. (2001) Three dimensional structure of Photosystem I at 2.5 Å resolution, *Nature 411*, 909−917.
19. Ishikita, H., and Knapp, E. W. (2003) Redox potential of quinones in both electron transfer branches of Photosystem I, *J. Biol. Chem. 278*, 52002−52011.
20. Ivashin, N., and Larsson, S. (2003) Electron transfer pathways in Photosystem I reaction centers, *Chem. Phys. Lett. 375*, 383−387.
21. Shen, G., Antonkine, M. L., van der Est, A., Vassiliev, I. R., Brettel, K., Bittl, R., Zech, S. G., Zhao, J., Stehlik, D., Bryant, D. A., and Golbeck, J. H. (2002) Assembly of Photosystem I. II. Rubredoxin is required for the *in vivo* assembly of F_X in *Synechococcus* sp. PCC 7002 as shown by optical and EPR spectroscopy, *J. Biol. Chem. 277*, 20355−20366.
22. Shen, G., Zhao, J., Reimer, S. K., Antonkine, M. L., Cai, Q., Weiland, S. M., Golbeck, J. H., and Bryant, D. A. (2002) Assembly of Photosystem I. I. Inactivation of the *rubA* gene encoding a membrane-associated rubredoxin in the cyanobacterium *Synechococcus* sp. PCC 7002 causes a loss of Photosystem I activity, *J. Biol. Chem. 277*, 20343−20354.
23. Santabarbara, S., Heathcote, P., and Evans, M. C. (2005) Modelling of the electron transfer reactions in Photosystem I by electron tunnelling theory: the phylloquinones bound to the PsaA and the PsaB reaction centre subunits of PS I are almost isoenergetic to the iron-sulfur cluster F_X, *Biochim. Biophys. Acta 1708*, 283−310.
24. Antonkine, M. L., Jordan, P., Fromme, P., Krauss, N., Golbeck, J. H., and Stehlik, D. (2003) Assembly of protein subunits within the stromal ridge of Photosystem I. Structural changes between unbound and sequentially PS I-bound polypeptides and correlated changes of the magnetic properties of the terminal iron sulfur clusters, *J. Mol. Biol. 327*, 671−697.
25. Vassiliev, I. R., Yu, J. P., Jung, Y. S., Schulz, R., Ganago, A. O., McIntosh, L., and Golbeck, J. H. (1999) The cysteine-proximal aspartates in the F_X-binding niche of Photosystem I−effect of alanine and lysine replacements on photoautotrophic growth, electron transfer rates, single-turnover flash efficiency, and EPR spectral properties, *J. Biol. Chem. 274*, 9993−10001.
26. van der Est, A., Valieva, A. I., Kandrashkin, Y. E., Shen, G., Bryant, D. A., and Golbeck, J. H. (2004) Removal of PsaF alters forward electron transfer in Photosystem I: Evidence for fast reoxidation of Q_KA in subunit deletion mutants of *Synechococcus* sp. PCC 7002, *Biochemistry 43*, 1264−1275.
27. Gerken, S., Brettel, K., Schlodder, E., and Witt, H. T. (1987) Direct observation of the immediate electron-donor to chlorophyll-a_{II} ($P680^+$) in oxygen-evolving Photosystem-II complexes−Resolution of nanosecond kinetics in the UV, *FEBS Lett. 223*, 376−380.

28. Brettel, K., and Schlodder, E. (1988) $Ru(bipy)_3Cl_2$ luminescence as optical step signal for detector testing, *Rev. Sci. Instrum. 59*, 670−671.
29. Kohlrausch. (1854) Theorie des elektrischen Rückstandes der Leidner Flasche, *Poggendorf's Annalen der Physik und Chemie 91*, 56−82.
30. Kohlrausch. (1863) Über die elastiche Nachwirkung bei der Torsion, *Poggendorf's Ann. Phys. Chem. 119*, 337−368.
31. Schlodder, E., Falkenberg, K., Gergeleit, M., and Brettel, K. (1998) Temperature dependence of forward and reverse electron transfer from A_1^-, the reduced secondary electron acceptor in Photosystem I, *Biochemistry 37*, 9466−9476.
32. McMahon, B. H., Muller, J. D., Wraight, C. A., and Nienhaus, G. U. (1998) Electron transfer and protein dynamics in the photosynthetic reaction center, *Biophys. J. 74*, 2567−2587.
33. Vassiliev, I. R., Kjaer, B., Schorner, G. L., Scheller, H. V., and Golbeck, J. H. (2001) Photoinduced transient absorbance spectra of $P840/P840^+$ and the FMO protein in reaction centers of *Chlorobium vibrioforme*, *Biophys. J. 81*, 382−393.
34. Brooks, B. R., Bruccoleri, R. E., Olafson, B. D., States, D. J., Swaminathan, S., and Karplus, M. (1983) CHARMM: a program for macromolecular energy minimization and dynamics calculations, *J. Comput. Chem. 4*, 187−217.
35. Sebban, P., Maróti, P., Schiffer, M., and Hanson, D. K. (1995) Electrostatic dominoes: long distance propagation of mutational effects in photosynthetic reaction centers of *Rhodobacter capsulatus*, *Biochemistry 34*, 8390−8397.
36. Axelrod, H. L., Abresch, E. C., Paddock, M. L., Okamura, M. Y., and Feher, G. (2000) Determination of the binding sites of the proton transfer inhibitors Cd^{2+} and Zn^{2+} in bacterial reaction centers, *Proc. Natl. Acad. Sci. U.S.A. 97*, 1542−1547.
37. Ishikita, H., and Knapp, E.-W. (2005) Induced conformational change upon Cd^{2+} binding at photosynthetic reaction centers, *Proc. Natl. Acad. Sci. U.S.A. 102*, 16215−16220.
38. Ishikita, H., Stehlik, D., Golbeck, J. H., and Knapp, E. W. (2006) Electrostatic influence of PsaC protein binding to the PsaA/PsaB heterodimer in Photosystem I, *Biophys. J. 90*, 1081−1089.
39. MacKerell, A. D., Jr., Bashford, D., Bellott, R. L., Dunbrack, R. L., Jr., Evanseck, J. D., Field, M. J., Fischer, S., Gao, J., Guo, H., Ha, S., Joseph-McCarthy, D., Kuchnir, L., Kuczera, K., Lau, F. T. K., Mattos, C., Michnick, S., Ngo, T., Nguyen, D. T., Prodhom, B., Reiher, W. E., III, Roux, B., Schlenkrich, M., Smith, J. C., Stote, R., Straub, J., Watanabe, M., Wiorkiewicz-Kuczera, J., Yin, D., and Karplus, M. (1998) All-atom empirical potential for molecular modeling and dynamics studies of proteins, *J. Phys. Chem. B 102*, 3586−3616.
40. Davis, I. H., Heathcote, P., MacLachlan, D. J., and Evance, M. C. W. (1993) Modulation analysis of the electron spin echo signals of *in vivo* oxidised primary donor ^{14}N chlorophyll centers in bacterial, P870 and P960, and plant Photosystem I, P700, reaction centers, *Biochim. Biophys. Acta 1143*, 183−189.
41. Rigby, S. E. J., Heathcote, P., Evans, M. C. W., and Nugent, J. H. A. (1995) ENDOR and special TRIPLE resonance spectroscopy of $Q_A^{\bullet-}$ of Photosystem II, *Biochemistry 34*, 12075−12081.
42. Käss, H., and Lubitz, W. (1996) Evaluation of 2D-ESEEM data of ^{15}N-labeled radical cations of the primary donor P_{700} in Photosystem I and chlorophyll *a*, *Chem. Phys. Lett. 251*, 193−203.
43. Mac, M., Bowlby, N. R., Babcock, G. T., and McCracken, J. (1998) Monomeric spin density distribution in the primary donor of photosystem I as determined by electron magnetic resonance: functional and thermodynamic implications, *J. Am. Chem. Soc. 120*, 13215−13223.
44. Mouesca, J., Chen, J. L., Noodleeman, L., Bashford, D., and Case, D. A. (1994) Density functional/Poisson-Boltzmann calculations of redox potentials for iron-sulfur clusters, *J. Am. Chem. Soc. 116*, 11898−11914.
45. van der Est, A. (2001) Light-induced spin polarization in Type I photosynthetic reaction centers, *Biochim. Biophys. Acta 1507*, 212−225.
46. Ludwig, M. L., Pattridge, K. A., Metzger, A. L., Dixon, M. M., Eren, M., Feng, Y., and Swenson, R. P. (1997) Control of oxidation-reduction potentials in flavodoxin from *Clostridium beijerinckii:* the role of conformation changes, *Biochemistry 36*, 1259−1280.
47. Park, I. Y., Eidsness, M. K., Lin, I. J., Gebel, E. B., Youn, B., Harley, J. L., Machonkin, T. E., Frederick, R. O., Markley, J. L., Smith, E. T., Ichiye, T., and Kang, C. (2004) Crystallographic studies of V44 mutants of *Clostridium pasteurianum* rubredoxin: effects of side-chain size on reduction potential, *Proteins 57*, 618−625.
48. Käss, H., and Lubitz, W. (1996) Quadrupole parameters of nitrogen nuclei in the cation radical P_{700}^+ determine by ESEEM of single crystals of Photosystem I, *Chem. Phys. Lett. 257*, 197−206.
49. Breton, J., Nabedryk, E., and Leibl, W. (1999) FTIR study of the primary electron donor of photosystem I (P_{700}) revealing delocalization of the charge in $P_{700}^{\pm}$ and localization of the triplet character in $^3P_{700}$, *Biochemistry 38*, 11585−11592.
50. Breton, J., Xu, W., Diner, B. A., and Chitnis, P. R. (2002) The two histidine axial ligands of the primary electron donor chlorophylls $P_{700}^{\pm}$ in photosystem I are similarly perturbed upon $P_{700}^{\pm}$ formation, *Biochemistry 41*, 11200−11210.

BI700846Z